Landslides
DOI 10.1007/s10346-025-02659-9
Received: 22 July 2025
Accepted: 6 November 2025

Ondřej Racek · Andrea Morcioni · Jan Blahůt · Tiziana Apuani · Petr Štěpánek · Gianvito Scaringi

Atmospheric warming drives shallow rock slope instability via irreversible joint opening

Abstract Rock slopes are exposed to atmospheric temperature fluctuations, which affect the evolution of stresses and strains across various timescales. Climate change is modifying the thermal regime of rock masses, potentially accelerating processes associated with weathering and gravitational deformation. While current thermal and mechanical conditions of rock slopes can be monitored in situ, predicting their long-term evolution remains challenging. In this study, thermal and joint displacement data were used to calibrate a semi-coupled thermo-mechanical model of a rock slope at ***Pastýřská stěna*** in Děčín, Czechia. The model was then fed with projected temperatures over the next hundred years. Simulations showed progressive, irreversible joint opening and rock face displacement, suggesting increased instability in the slope's near-surface zone. These findings demonstrate that continued atmospheric warming in temperate climates may significantly impact the long-term stability of rock slopes, warranting systematic consideration of the role of thermal regimes at the atmosphere-ground interface.

Keywords Rock slope · Climate change · Thermo-mechanical model · Joint dynamic

Introduction

Atmospheric thermal loading on rock slope surfaces is increasingly recognised as a key preparatory factor for rockfall and slope instability (Collins and Stock 2016). Temperature-induced volume changes in rock mass blocks generate stresses that can encourage fracture initiation and growth (Eppes et al. 2016). Along with seismic shaking, pore water pressure fluctuations, freeze–thaw cycles, and root-induced stresses from vegetation growth, they contribute to irreversible joint deformation and ultimately shallow rock mass failure (Allen and Huggel 2013; Collins et al. 2018; Marmoni et al. 2020).

Joint displacements with diurnal, seasonal, and long-term patterns can be observed in response to temperature fluctuations (D'Amato et al. 2016; Mirhadi and Macciotta 2023). Although thermal effects appear minor at human timescales, their impact over geological timescales can be significant owing to their persistent and cyclic nature, which results in the accumulation of deformation and thermal fatigue (Hall 1999; Grämiger et al. 2018; Morcioni et al. 2022). Thermally induced rock slope destabilisation has been widely documented (Pasten et al. 2015; Guillemot et al. 2022); however, the underlying mechanisms remain insufficiently understood. Advanced monitoring systems and extensive in situ data collection have partially addressed this gap (Hormes et al. 2020; Blahůt and Racek 2023; Racek and Blahůt 2023). Monitoring of both near-surface (Brideau et al. 2011; Blikra and Christiansen 2014; Marmoni et al. 2020) and deep rock mass responses (Magnin et al. 2015; Fiorucci et al. 2018) has revealed the major role of thermal cycles operating on both short- and medium-term timescales, highlighting a strong link between atmospheric temperature fluctuations and deformation along discontinuities. Conversely, evaluating the long-term impacts of climatic changes remains challenging because of their gradual progression compared to the lifespan of monitoring systems (Harris et al. 2009; Mamot et al. 2021).

Numerical modelling is an important tool to investigate rock slope dynamics. It is widely employed in slope stability (Donati et al. 2020), failure mechanism and runout analysis (Fan et al. 2017; 2019; Deng et al. 2023; Zhao et al. 2024), and the assessment of mechanical parameters and strain forecasting in construction settings (Ravandi et al. 2013; Rafiee et al. 2018). Models incorporating thermal coupling have primarily focused on diffusive processes related to nuclear waste disposal (Zhou and Xu 2021; Tourchi et al. 2025) or geothermal energy extraction (Ozudogru et al. 2014). Few studies have focused on the thermo-mechanical nexus between climatic forcing and slope instability (Stoffel and Huggel 2012; Scaringi and Loche 2022), particularly in the context of jointed rock slopes (Lan et al. 2013; Marmoni et al. 2020; Wu et al. 2020; Salmon et al. 2023). Short-term temperature variations were first incorporated in slope stability assessments through simplified thermoelastic modelling (Gischig et al. 2011). Few studies have accounted for thermally induced strain accumulation and microcrack propagation (Wang et al. 2020; Wu et al. 2020; Yu et al. 2023).

This study investigates the influence of climate change on thermally induced rock slope dynamics, focusing on irreversible joint displacement trends. Temperature cycles can act as both preparatory and triggering factors in slope destabilisation. While their role as a trigger can be accounted for relatively easily (Do Amaral Vargas et al. 2013; Gischig et al. 2016; Bolla and Paronuzzi 2020), modelling temperature-driven preparatory processes is complex owing to the longer timescale over which they act and their dependence on rock mass properties. Precise calibration of both thermal and mechanical parameters is essential. Thus, a multi-step calibration workflow was developed. The focus was on the ***Pastýřská stěna*** rock slope in Czechia, where in situ monitoring of meteorological variables, rock mass temperatures, and joint displacements has been operating since 2018 (Racek et al. 2021).

Study area

The sandstone rock slope known as ***Pastýřská stěna*** (the Shepherd's Wall) is situated on the left bank of the Elbe River in Děčín, northwestern Czechia (Fig. 1a). The slope is composed of Turonian sandstone (Cílek, 2009) (Fig. 1b) and belongs to the Bohemian

Published online: 25 November 2025

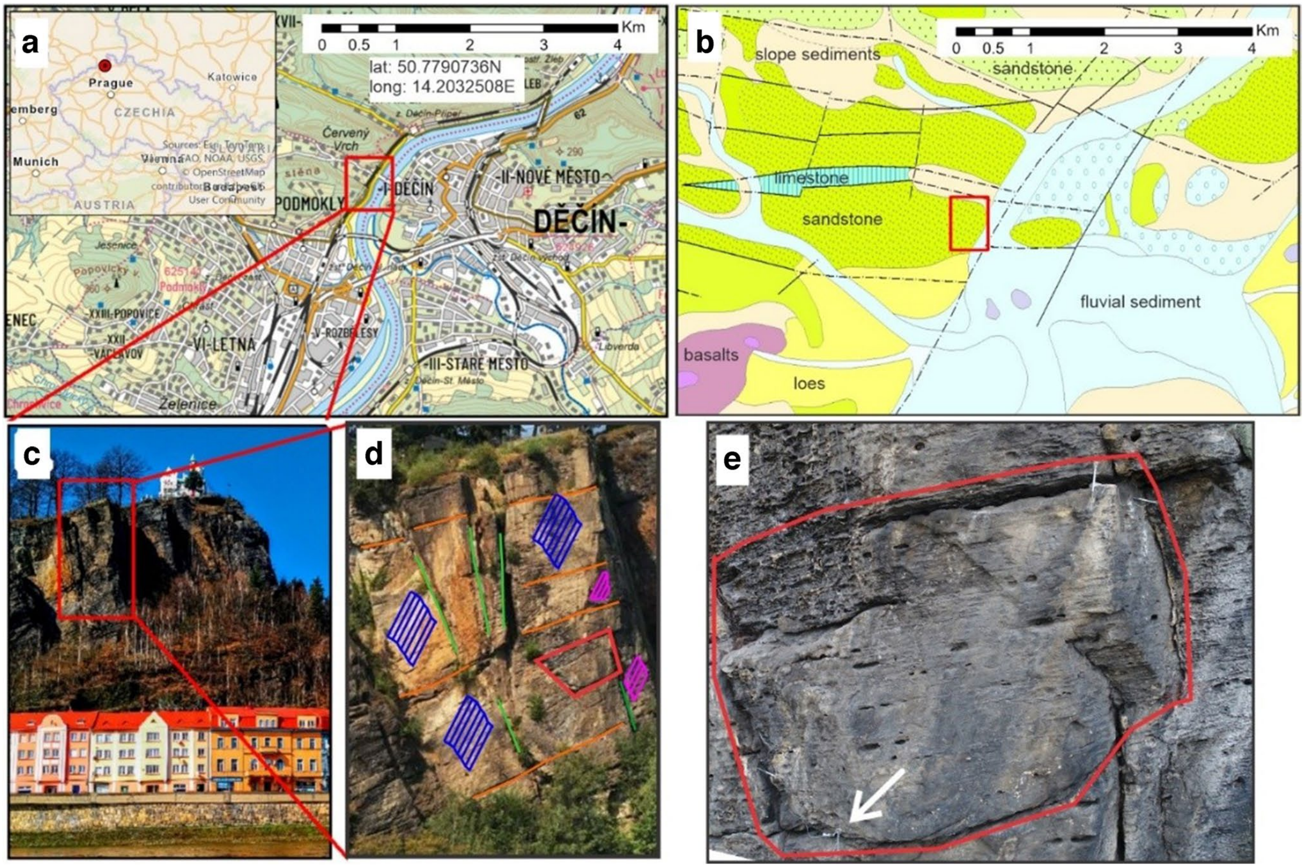

Fig. 1 Study area. (**a**) Location of the ***Pastýřská stěna*** rock slope in Děčín (marked by a red rectangle), northwestern Czech Republic (red dot in the inset). (**b**) Simplified geological map of the surrounding area. (**c**) Distant view of ***Pastýřská stěna***. (**d**) Close-up view of the rock slope; the monitored rock block is outlined in red, and the mapped discontinuity sets are indicated as: J1, green lines; J2, blue polygons; J3, magenta polygons; J4, orange lines. (**e**) Detailed view of the monitored block, where the position of the crack meter is indicated by a white arrow

Cretaceous Basin (Čech 2011), with an overall south-east-facing orientation. Geomorphologically, it is a prominent example of a cuesta. The slope was formed by fluvial erosion during the uplift associated with the Alpine orogeny. The site has a documented history of rockfalls (Zajíc 1977; Vařilová et al. 2022), which led to stabilisation measures being implemented in the late 1980s. Its proximity to residential buildings (Fig. 1c) justified the need for continuous monitoring. The site was thus selected owing to the availability of long-term climatic data, subsurface rock temperature time series, and joint deformation measurements.

Characterisation

Fieldwork was conducted to characterise the structural and geomechanical properties of the rock mass. Surface deformation was monitored using an linear potentiometric crackmeter installed across an open joint (Fig. 2b). A dense point cloud (DPC) of the slope was generated from Unmanned Aerial Vehicle (UAV) imagery combined with Structure-from-Motion (SfM) photogrammetry (Fig. 2a). Ground control points (GCPs) were employed for accurate georeferencing. The DPC was used to extract the slope geometry and identify discontinuity sets (Fig. 2c) via DSE software (Riquelme et al. 2016) and CloudCompare. A 3D model was constructed after trimming the DPC down to several hundred points while preserving the surface morphology.

Owing to the slope's limited accessibility, characterising the joint network required both direct and indirect methods. Four main discontinuity sets were identified during field campaigns and corroborated by DPC analysis; spacing and persistence were classified according to ISRM recommendations (1978):

- J1: 80°/40°; spacing: 8 ± 0.5 m; persistence: 80% ~ 11 m (high persistence);
- J2: 86°/320°; spacing: 7 ± 1 m; persistence: 50% ~ 6 m (medium persistence);
- J3: 85°/275°; spacing: 7.5 ± 0.5 m; persistence: 20% ~ 2 m (low persistence);
- J4: 30°/180°; spacing: 0.7 ± 0.1 m; persistence: 60%.~ 9 m (medium persistence).

Comparing the results of direct field mapping with those of indirect, automated methods (Fig. 2d) highlighted the greater dispersion of orientations found with the latter, possibly owing to the larger coverage. In fact, the extensive outcrop cannot be fully

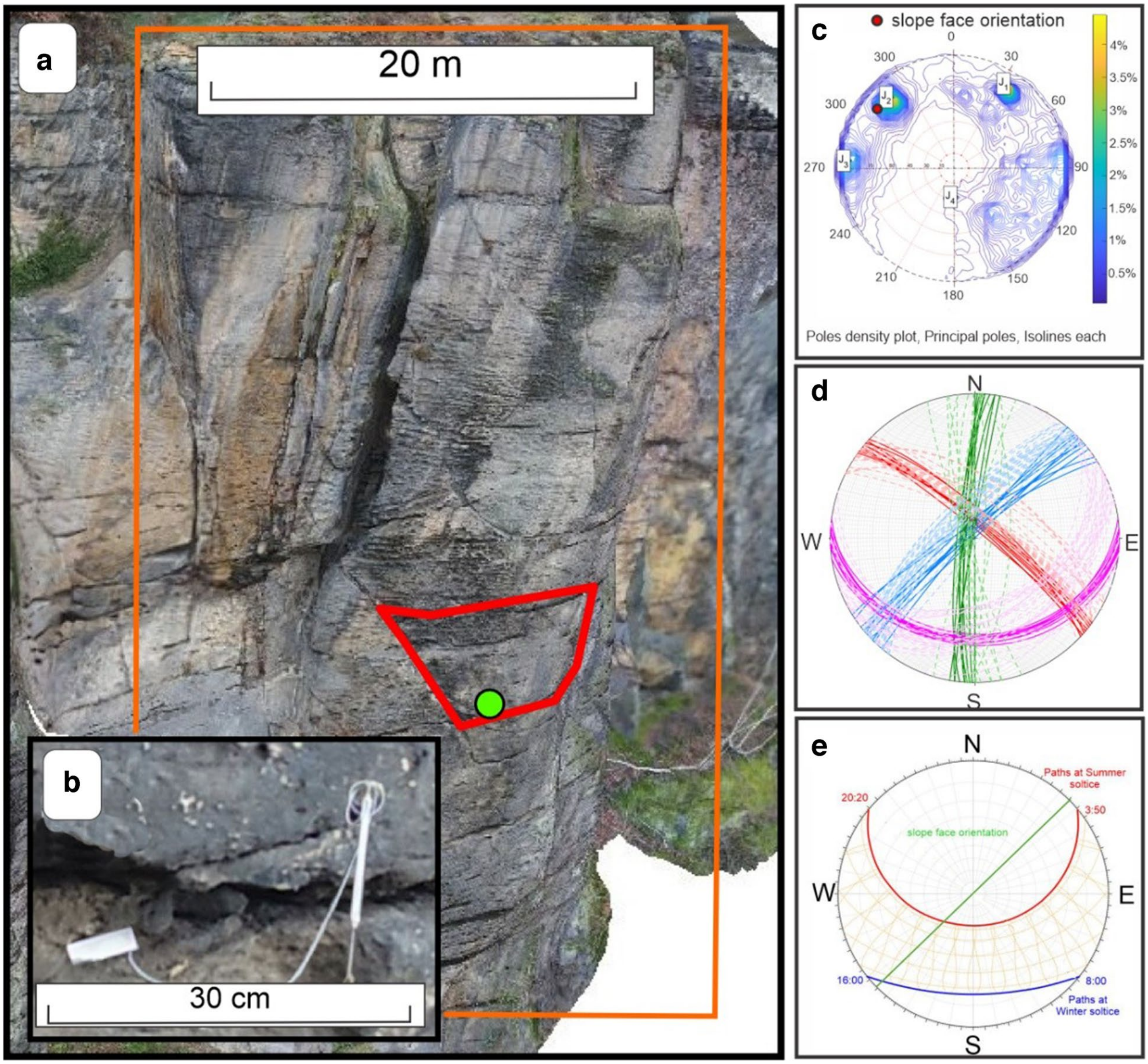

Fig. 2 ***Pastýřská stěna*** rock slope: geomechanical features and 3D point cloud. (**a**) Detail of the UAV-derived point cloud used for constructing model geometries. The red polygon marks the monitored block used for model calibration; the orange rectangle indicates the extent of the whole-slope predictive model geometry. The green dot shows the crackmeter location. (**b**) Close-up of the induction crackmeter installed across a joint. (**c**) Lower-hemisphere stereographic projection showing the pole density distribution. The four main discontinuity sets are labelled J1 to J4. (**d**) Comparison of in-field mapped (solid lines) and automatically derived planes (dashed lines): J1, red; J2, blue; J3, green; J4, magenta. (**e**) Solar path diagram for the study site, with a reference line indicating the orientation of the slope face

explored through field inspection. Nevertheless, the comparison shows a satisfactory agreement for all mapped joint sets.

Representative weathered and unweathered boulders were collected at the base of the rock wall, from which cylindrical samples were prepared and submitted to testing. Ten samples were analysed via non-destructive ultrasonic testing to determine dynamic mechanical properties (Table S1, see Supplementary material). Seismic wave velocities (V_p, V_s) were measured axially in all specimens. Uniaxial compressive strength (UCS) was evaluated on ten samples, following ASTM D3148 (ASTM 2002) (Table 1). Direct sampling of discontinuities was unfeasible; thus, joint properties were estimated from the literature (Barton 1976; Hoek and Brown 1997; Wyllie and Mah 2017).

The values obtained from laboratory testing and literature served as a reference for model calibration. Strength and deformability parameters of the intact samples appeared relatively low, with destructive tests indicating a pronounced reduction in mechanical performance associated with increasing weathering. This reduction is likely influenced by the sampling location—at the toe of the slope—where rocks may be more exposed to weathering. Consequently, the measured properties may not fully represent the overall characteristics of the slope, suggesting the need for careful

Table 1 Average values and standard deviations of the sandstone's mechanical parameters, obtained from UCS testing. UCS: uniaxial compressive strength, E: Young's modulus, G: shear modulus, K: bulk modulus, ν: Poisson's ratio

Sample type	UCS [MPa]	E [GPa]	G [GPa]	K [GPa]	ν
Unweathered	24.85 ∓ 2.19	15.68 ∓ 0.93	6.55 ∓ 0.27	8.68 ∓ 1.29	0.2 ∓ 0.02
Weathered	8.53 ∓ 2.75	3.88 ∓ 1.46	1.70 ∓ 0.57	4.07 ∓ 0.17	0.32 ∓ 0.06
All samples	18.32 ∓ 8.36	10.96 ∓ 5.90	4.93 ∓ 2.32	7.14 ∓ 2.42	0.24 ∓ 0.07

calibration in the numerical modelling phase. Moreover, the inherent heterogeneity of sandstone further complicates the definition of a single, representative set of mechanical parameters for the entire slope. To confirm the underestimation of the mechanical properties of the samples, four blocks at the foot of the slope and four surfaces directly on the rock slope were tested using a Schmidt hammer (Table S3, see Supplementary material). If we compare the average Schmidt hammer rebound, its value is 13% higher in the case of the rock slope surface.

Monitoring

The site has been monitored since 2018 by a system consisting of meteorological, thermal, and mechanical components (Racek et al. 2021).

The long-term average air temperature at the site is 12.5 °C, with recorded extremes ranging from − 12.6 to 41.9 °C (amplitude: 54.5 °C). The thermal monitoring system consists of a 3-m-deep horizontal borehole instrumented with 12 thermocouples installed at 0.05, 0.1, 0.2, 0.3, 0.5, 0.75, 1.0, 1.5, 2.0, 2.5, and 3-m depths. The borehole was drilled into a rock slab with no visible open joints, and the probe was thermally insulated at both the head and between thermocouples to minimise heat exchange. Surface temperature is also monitored using an external thermocouple. Observations show an average rock surface temperature of 14.1 °C, gradually decreasing to 13.4 °C at 3-m depth. Diurnal temperature fluctuations are detectable down to 75 cm during warmer months, while annual temperature variations are observable across the full 3-m depth. The annual temperature amplitude reaches up to 41 °C at the surface and reduces to 12 °C at 3 m. Monthly averaged data from the thermal probe were used to calibrate the thermal properties of the rock matrix.

Mechanical monitoring relies on linear potentiometric crackmeters. Each device has a 200-mm range and 0.05-mm resolution. The crackmeter used for model calibration is oriented perpendicular to a sub-horizontal joint belonging to set J4 (the sandstone's stratification layers, Fig. 2b). During monitoring, it recorded an average position of 99.3 mm, with 1.315-mm annual displacement amplitude. No significant long-term opening/closing trend was observed.

To assess the impact of climate change on the thermally driven dynamics of the slope's surficial zone, predictions of future temperature conditions are required. Temperature data were derived from a 500-m resolution regional climate model for Czechia (Meitner et al. 2023), based on the CMIP6 global climate model ensemble. Seven representative global models were selected for downscaling, producing monthly mean temperature projections for multiple future climate periods. The model provided averaged data for 30-year time windows: M23 (1995–2025), M25 (2011–2022), M35 (2021–2050), M45 (2031–2060), M55 (2041–2070), M65 (2051–2080), and M75 (2061–2090). Two temperature increase scenarios were considered (Fig. S1). The first scenario uses the mean expected temperatures for each time period, while the second incorporates the 95th percentile values, representing a high-emissions or accelerated warming pathway. For both scenarios, monthly temperature time series were derived for all future periods (M23–M75). As the temporal resolution of the climatic model is one month, the simulations are limited to capturing annual thermal cycles, without accounting for short-term (e.g., diurnal) variations.

Numerical modelling

Modelling was conducted in two steps. Initial thermal calibration was done in COMSOL Multiphysics 5.4. Then, more complex simulations were developed in 3DEC 9.0, where the rock mass was represented as an assemblage of deformable blocks. These were internally discretised using a finite-difference mesh and governed by a user-defined linear or nonlinear stress–strain constitutive law. Rock joints were treated as mechanical interfaces between intact blocks, capable of transmitting normal and shear forces. If the imposed stress conditions exceeded the defined strength parameters, joint failure was initiated, allowing for relative displacement between blocks.

A thermo-mechanical semi-coupled modelling approach was applied to evaluate the influence of annual temperature fluctuations on the stress–strain evolution of the slope. Transient temperature fields were computed within 3DEC using the heat conduction equation:

$$\frac{\partial T}{\partial t} = \frac{\lambda}{\rho C_V}\left(\frac{\vartheta^2 T}{\partial X^2} + \frac{\vartheta^2 T}{\partial Y^2} + \frac{\vartheta^2 T}{\partial Z^2}\right) \quad (1)$$

where λ is the thermal conductivity, ρ is the rock bulk density and C_V is the heat capacity.

To analyse the effects of temperature variations on the stress–strain field, a linear thermoelastic behaviour was assumed for the rock mass. The thermoelastic response of the intact rock is governed by four parameters: Young's modulus (E), Poisson's ratio ν, thermal expansion coefficient (α), and bulk density (ρ).

The mechanical behaviour of the discontinuities was modelled using Mohr–Coulomb's failure criterion, which requires the definition of joint normal stiffness (K_N), shear stiffness (K_S), internal friction angle (φ), and cohesion (c).

In the thermal domain, heat conduction through the rock matrix is characterised by two parameters: thermal conductivity

(λ) and specific heat capacity (C_P). Together, these define the thermal diffusivity (D):

$$D = \frac{\lambda}{\rho C_P} \tag{2}$$

Values of $\lambda = 2.5$–3.5 W m^{-1} K^{-1} and $C_P = 500$–750 J kg^{-1} K^{-1} were adopted based on relevant literature (Desai et al. 1974; Sundberg 1988; Balkan et al. 2017; Emirov et al. 2021). In the model, variations in the stress state are thus induced by thermal strains caused by the isotropic volumetric expansion or contraction of the rock blocks. This thermal strain is computed as:

$$\Delta\sigma_{ij} = \delta_{ij} 3K\alpha\Delta T \tag{3}$$

where $\Delta\sigma_{ij}$ is the change in stress, δ_{ij} is Kronecker's delta, K is the bulk modulus, and ΔT is the temperature change.

For each block in the model, thermally induced volumetric strains—resulting from surface temperature variations—lead to changes in the local stress state. These strains are constrained by the adjacent blocks on all sides except the exposed slope face. As a consequence, stress changes may propagate to depths beyond the so-called ***thermally active layer***, defined as the maximum depth at which surface temperature variations exert measurable effects. These stress variations affect the discontinuities (block interfaces), where elastoplastic behaviour is assumed. When the evolving shear stress at an interface exceeds its strength, plastic strain occurs.

Calibration

A multi-step calibration process was used, starting with simple conceptual models and gradually adding more geometric and physical complexity. This approach enables efficient parameter tuning at lower computational costs and produces more realistic values in the final, full-scale model. The parameters from the most advanced calibration stage served as representatives of the actual in situ conditions. After calibration, a more complex model—the ***whole-rock slope predictive model*** (WRSPM)—was implemented to simulate the slope's behaviour under future atmospheric temperature scenarios. The complete modelling workflow is illustrated in Fig. 3.

To calibrate the rock matrix's thermal and mechanical parameters, three increasingly complex geometries were employed (Fig. S2): a preliminary ***Borehole model*** for 1D thermal calibration, a simplified 3D ***Blocky model*** for both thermal and mechanical calibration, and a refined 3D ***Topo model***, representing a more realistic conceptual volume of a part of the slope, used for advanced thermal and mechanical calibration.

For thermal calibration, monthly average rock mass temperatures recorded by the compound borehole probe were used. Surface temperatures, averaged monthly, were applied as boundary conditions to the model's upper surface. The thermal properties of the rock matrix were then adjusted iteratively until a good agreement was reached between modelled and measured temperatures at all monitored depths.

Mechanical calibration relied on the time series of joint displacements obtained from the surface-mounted crackmeter. The modelled normal displacement across the discontinuity was compared to the observed displacement. Both rock matrix mechanical properties and discontinuity parameters were adjusted until a satisfactory correspondence between modelled and measured displacements was achieved.

For each calibration step, the coefficient of determination R^2 was calculated. The quality of the model calibration was expressed using the root mean square error (RMSE) and normalised RMSE (NRMSE):

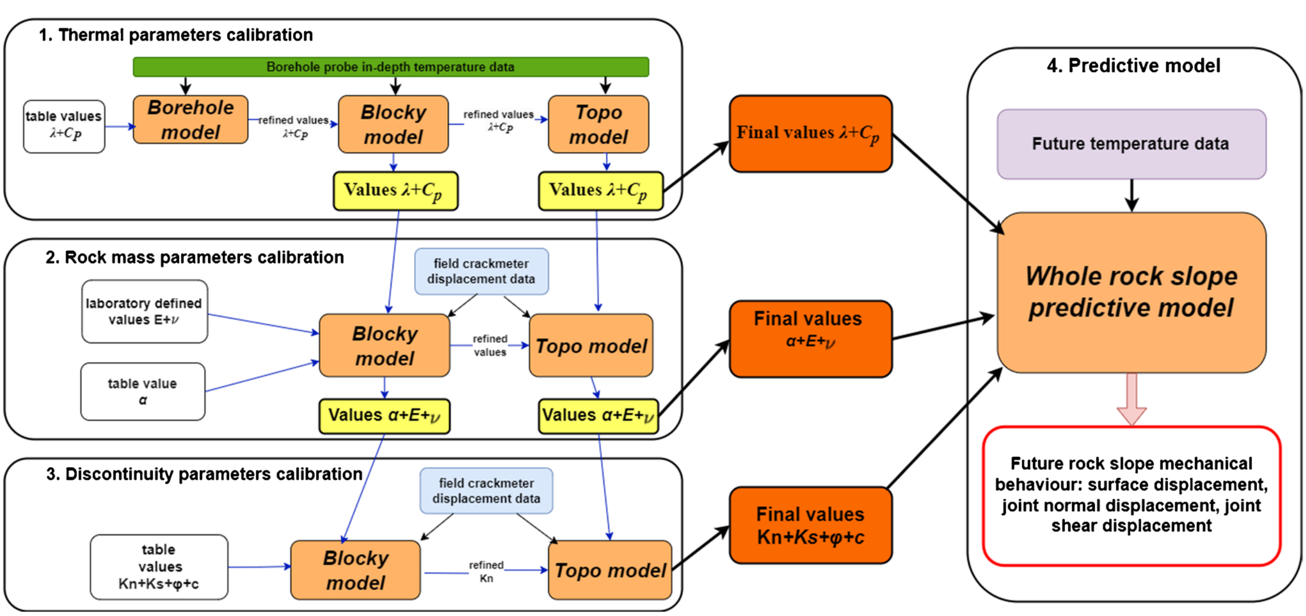

Fig. 3 Modelling workflow

$$\mathrm{RMSE} = \sqrt{\frac{\sum_{i=1}^{n}(V_m - V_s)^2}{n}} \quad (4)$$

$$\mathrm{NRMSE} = \frac{\mathrm{RMSE}}{V_{max} - V_{min}} \quad (5)$$

where V_m is the measured value of temperature or joint displacement, and V_s is the simulated value. Lower RMSE values indicate a better fit. For NRMSE, values < 0.5 are generally considered to represent a good model fit.

The geometries used in each modelling step and the related modelling procedure are described in detail in Text S1 in the Supplementary material file.

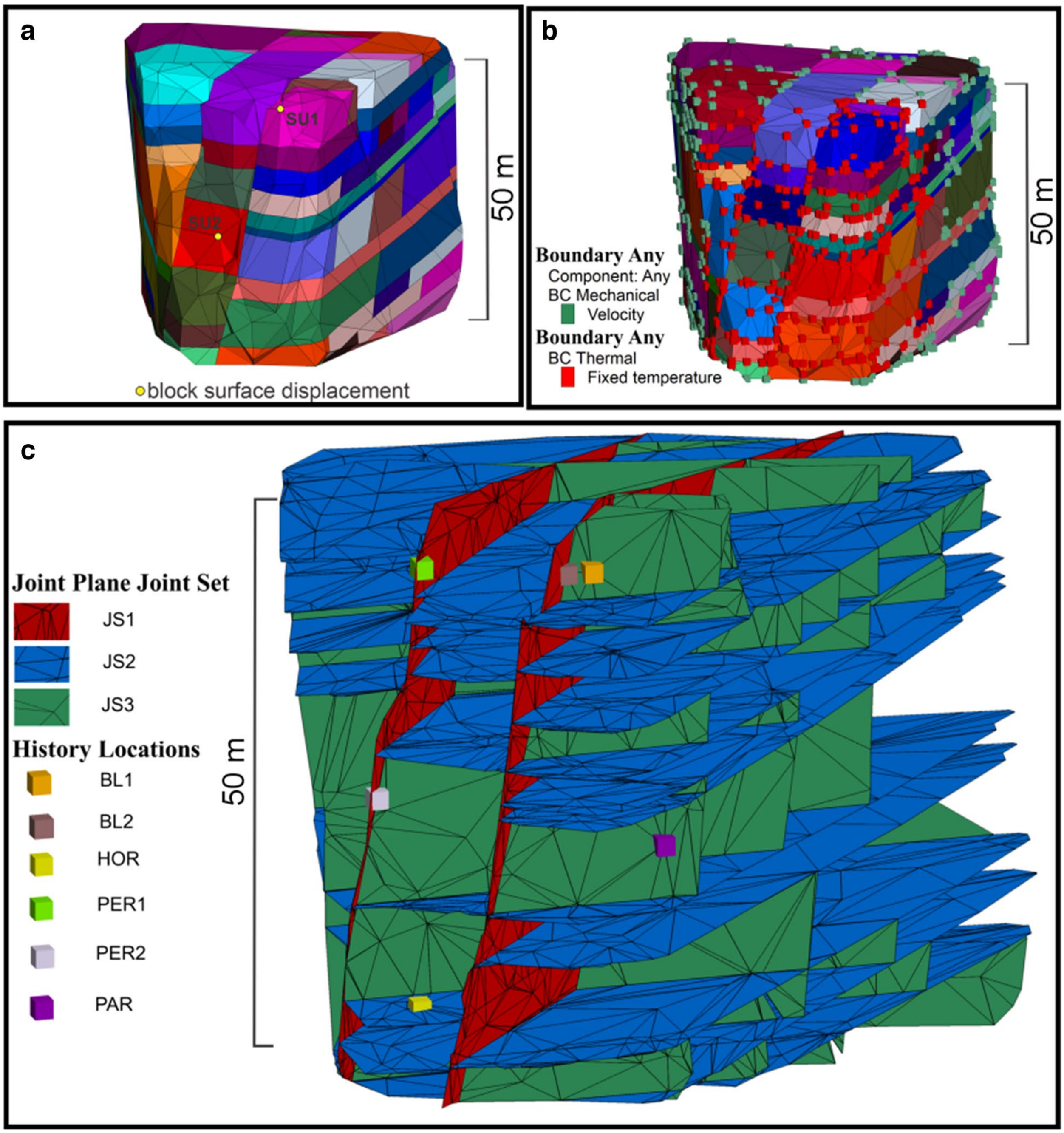

Fig. 4 Whole-rock slope predictive model (WRSPM). (**a**) Geometry of the model domain, showing the location of surface displacement history points. (**b**) Model boundary conditions: green cubes indicate points with fixed velocities. Red cubes mark points with fixed temperature during month-long time steps. (**c**) Generalised joint network implemented in the model, with history points positioned at key locations within the discontinuities, monitoring joint normal and shear displacement

Prediction

The conceptual WRSPM domain represents the ***Pastýřská stěna*** rock slope in its actual scale (60 × 60 × 80 m) and geometry (Fig. 4), corresponding to the northeastern sector of the slope, where surface displacements are being monitored. The joint network is represented by three discontinuity sets, modelled with a 5% dispersion in orientation: JS1, 80/40, spacing 8 ± 1 m, persistence 80%; JS2, 30/180, spacing 7 ± 1 m, persistence 60%; JS3, 86/320, spacing 0.7 ± 0.1 m, persistence 50%. An additional set identified in the field (J3, 85/275) was not included as it is only marginally present within the modelled domain and is poorly developed.

Initial thermal and mechanical rock properties used in the WRSPM were adopted from the calibrated ***Topo model***: $\lambda = 2.75$ $W{\cdot}m^{-1}{\cdot}K^{-1}$, $C_P = 520$ $J{\cdot}kg^{-1}{\cdot}K^{-1}$, $\alpha = 1.15 \times 10^{-5}$ m/m·°C, E = 3.0 GPa, $\nu = 0.25$, and $\rho = 2.1$ g/cm3. Joint parameters were set as: $K_N = 1.9$ GPa, $K_S = 1.2$ GPa, $\varphi = 30°$, and c = 0.1 MPa.

Mechanical boundaries were set to zero velocity at the sides and bottom of the model domain, corresponding to deeper sections of the slope where no thermal or mechanical activity is expected. The topographical surface and top of the domain remained unconstrained, simulating the free surface conditions of the actual rock slope. Thermal boundaries were defined using varying monthly average temperatures—based on climate model projections—applied to the topographical surface. The remaining boundaries (upper and bottom faces at depth) were assigned the condition Q = 0, indicating no heat flux.

An initial elastic stress field was computed through mechanical initialisation. Initially, the discontinuity strength parameters (cohesion and friction angle) were increased by one order of magnitude to prevent failure, and the elastic stress field was computed until force equilibrium was achieved. The resulting displacements after initialisation were reset to isolate thermally induced changes. Subsequently, a one-year simulation using current average monthly temperatures was performed to establish a realistic initial temperature distribution within the rock mass. This thermal initialisation ensures that the starting thermal profile reflects in situ conditions.

During the model run, displacements were recorded at two surface points (SU1 and SU2; Fig. 4a) and six joint-embedded points (Fig. 4c). These history points enabled the monitoring of temporal and spatial responses of the rock mass and joints to thermal forcing:

- SU1, SU2: surface displacements.
- BL1, BL2: normal and shear displacements within joint sets JS1 and JS3, respectively. BL2 is located at the intersection of JS1 and JS3.
- HOR: monitors both shear and normal displacement in sub-horizontal joint set JS2.
- PER1: within the sub-vertical joint set JS1, perpendicular to the slope surface.
- PER2: located at the intersection of JS1 and JS3.
- PAR: within JS3, which is sub-parallel to the slope surface.

The model was subjected to monthly average temperatures projected for future climate scenarios. Seven future periods (M23 to M75) were simulated as a 1-year model step with 12 monthly temperature values. This resulted in seven consecutive "conceptual years" of rising temperature, with M75 representing the climate of 2061–2090. As such, warming was significantly accelerated, but the number of temperature cycles in the model was reduced. Although compressed in time, the simulation conceptually spans 70 years of expected warming.

To assess the impact of temperature rise, three simulations were performed following the temperature initialisation stage. In all cases, the initial temperature of the rock mass was defined by running the annual model with average monthly temperatures from 1991–2020. Three hypotheses were explored.

- PH_NW (no warming): simulated seven years using the current climate state (M23); assumes no temperature increase ($\Delta T = 0$ °C).
- PH_C (climate warming – central estimate): Simulated seven consecutive years representing future periods M23 to M75, using the central estimate of monthly temperature projections ($\Delta T = 0.33$ °C in 30 years). Each step built upon the previous year's results.
- PH_C95 (high warming – 95th percentile): Similar to PH_C but driven by the upper 95th percentile of projected temperatures ($\Delta T = 0.56$ °C in 30 years), representing an accelerated warming scenario.

Results

Calibration

A summary of the calibrated thermal and mechanical parameters is provided in Table 2. For each calibration step, the thermal and mechanical responses at designated history points were compared with the measured average temperatures and joint displacements. The results of the thermal simulation using the ***Borehole model*** are presented in Fig. 5, with reference to depths of 5, 150, and 300 cm over a 4-year period. The simulation demonstrates a high level of agreement, with the average temperature difference between the modelled and measured data being less than 1 °C. This strong coherence is further supported by the low RMSE and NRMSE values. The best fit was obtained with $\lambda = 2.9$ m^{-1} K^{-1} and $C_P = 500$ J kg^{-1} K^{-1}.

These thermal parameters were then applied to the ***Blocky model*** to refine the thermal calibration and initial mechanical calibration. Simulated temperatures at 1, 2, and 3-m depths were compared with measured monthly average temperatures during 2020–2021 (Fig. S4). The best fit was achieved with $\lambda = 2.75$ m^{-1} K^{-1} and $C_P = 500$ J kg^{-1} K^{-1}. Average differences between modelled and measured monthly temperatures within 0.22 °C were achieved.

Mechanical calibration provided $\alpha = 1.10{\cdot}10^{-5}$ m/m °C and $K_N = 2.1$·GPa. However, some discrepancy between the modelled and measured joint displacements remained (Fig. 5), attributable to model simplifications. In fact, the rock matrix was assumed homogeneous and without microcracks, and the model was driven by monthly average surface temperatures. The maximum discrepancy was 0.013 mm, corresponding to a relative deviation $\Delta_{meas}/\Delta_{mod} = 16.5\%$. Nevertheless, high R^2 and low RMSE and NRMSE values were evaluated.

Thermal parameters from the calibrated ***Blocky model*** were input into the ***Topo model***. Owing to the more complex geometry,

Table 2 Thermal and mechanical parameters of the ***Pastýřská stěna*** rock slope resulting from calibration. λ = thermal conductivity; C_p = heat capacity; α = linear thermal expansion coefficient; E = Young's modulus; ν = Poisson's ratio; K_N = joint normal stiffness

Model	*Borehole model* T-simulation	*Blocky model* T-simulation	*Blocky model* T/M-simulation	*Topo model* T-simulation	*Topo model* T/M-simulation
Geometry	1D line	3D domain		3D detailed domain (topographic surface)	
Properties					
λ [$W·m^{-1}·K^{-1}$]	2.9	2.75	-	2.75	-
C_p [$J·kg^{-1}·K^{-1}$]	500	500	-	520	-
α [m/m °C]	-	-	1.10E^{-5}	-	1.15E^{-5}
E [GPa]	-	-	-	-	30.0
ν	-	-	-	-	0.25
K_N [GPa]	-	-	2.1	-	1.9

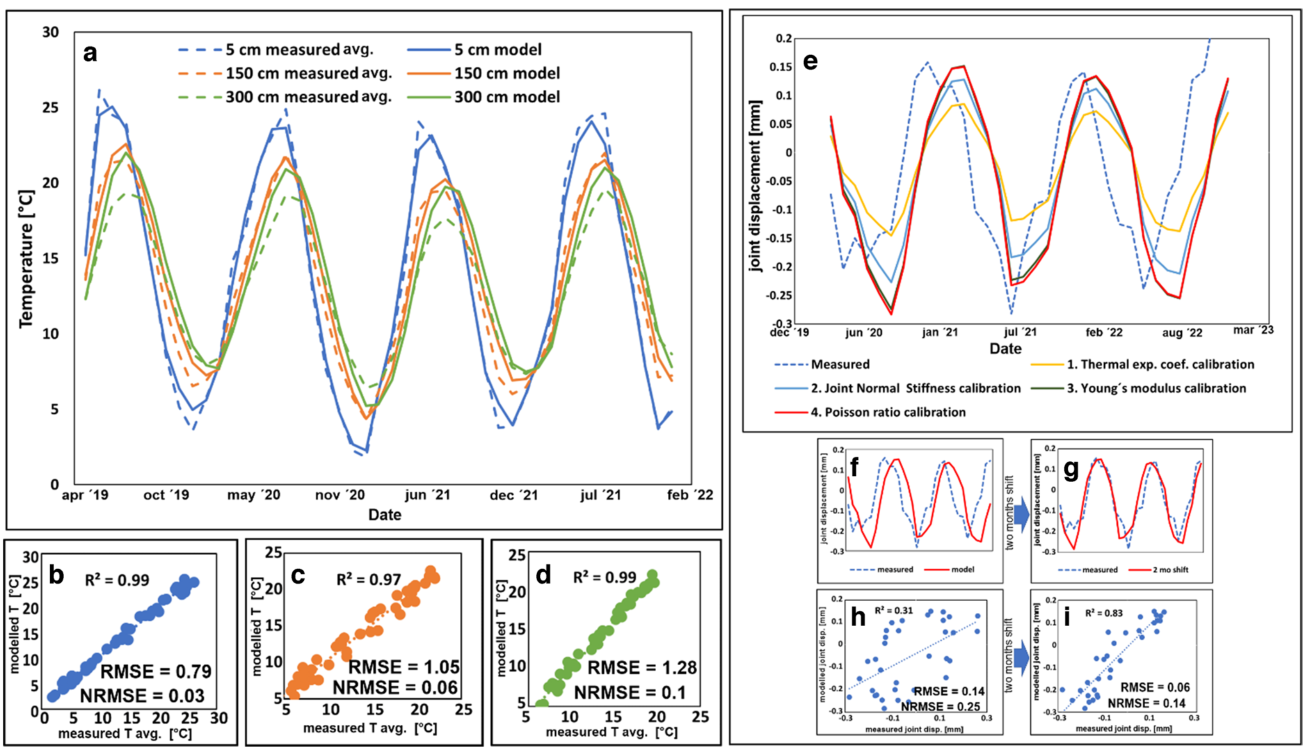

Fig. 5 Thermal calibration of the ***Borehole model*** and mechanical calibration of ***Topo model***. (**a**) Monthly-averaged measured temperatures (dashed lines) (Racek et al. 2021) and modelled temperatures (solid lines) at different depths. Linear regressions, R^2, RMSE, and NRMSE values at depths of 5 cm (**b**), 150 cm (**c**), and 300 cm (**d**), (**a**) Comparison of modelled and measured joint displacement throughout all stages of the mechanical calibration process. (**f–h**) Modelled vs. measured joint displacement before applying a temporal shift: (**f**) displacement curves showing a temporal misalignment; (**h**) corresponding statistical evaluation using R2, RMSE, and NRMSE. (**g–i**) Modelled vs. measured joint displacement after temporal shift correction: (**g**) Improved alignment of displacement curves. (**i**) Updated model performance metrics showing enhanced fit

calibration was only possible for the history point at 3-m depth. The amplitudes and discrepancies between the modelled and in situ measured temperatures were compared for the period March 2020–December 2021. The best fit was achieved for $\lambda = 2.75\ m^{-1}\ K^{-1}$ and $C_P = 520\ J\ kg^{-1}\ K^{-1}$, resulting in a difference in temperature amplitude of just 0.3 °C (Fig. S6).

To improve the calibration of mechanical parameters, joint displacements recorded between March 2020 and December 2023 were simulated using the ***Topo model*** (Fig. S7). A temporal shift was observed between the modelled and measured joint displacements, attributable to simplifications in both the model domain and the geometry of the monitored rock block, as well as to the assumption of a homogenous rock matrix. The best-fitting simulation was obtained with $\alpha = 1.15 \cdot 10^{-5}$ m/m °C, $K_N = 1.9$ GPa, $E = 3.0$ GPa, and $\nu = 0.25$. A difference in joint displacement amplitude of 0.07 mm and an average difference between the modelled and measured displacements of 0.025 mm were attained. The maximum relative error $\Delta_{meas}/\Delta_{mod}$ was 24.6%, which decreased to ~13% after temporally aligning the data series (Fig. S7b,d).

Notably, when the combination of thermal parameters is appropriately selected, the shape of the modelled temperature curve closely matches the measured data. However, the mechanical models exhibit high sensitivity to the coefficient of thermal expansion (α), where even minor adjustments can result in substantial changes in the modelled joint displacement. Young's modulus (E) primarily controls the amplitude of annual displacement cycles, influencing both the maximum expansion and contraction peaks. The normal stiffness of the discontinuity (K_N) has a direct effect on joint closure during warm periods, as it governs the resistance of the joint to compression. Higher values of K_N result in reduced joint closure during thermal expansion phases.

Prediction

The WRSPM results are presented as temporal displacement graphs. Displacement evolution was monitored throughout the simulation period at designated history points, covering all seven future time intervals (M23–M75). In particular, the displacement of two surface history points, SU1 and SU2, was monitored (Fig. 6). The former represents the displacement of the highest part of the rock slope, corresponding to a free-standing partial block; the latter captures the temporal displacement of the surficial partial block in the lower portion of the slope.

For each annual temperature cycle, two peaks of surface displacement are observed at both history points (Fig. 6a, b). The amplitude and overall trend are more pronounced at SU1, suggesting that the upper part of the slope, represented by a partially detached block, is more susceptible to thermal forcing. Notably, under the PH_C95 scenario, a more intense temperature increase results in an amplified displacement trend across the entire modelled slope face.

The overall maps (Fig. 6c) highlight displacement concentration in the upper right portion of the domain (up to ~12 mm), which reflects a combination of gravitationally driven block movement

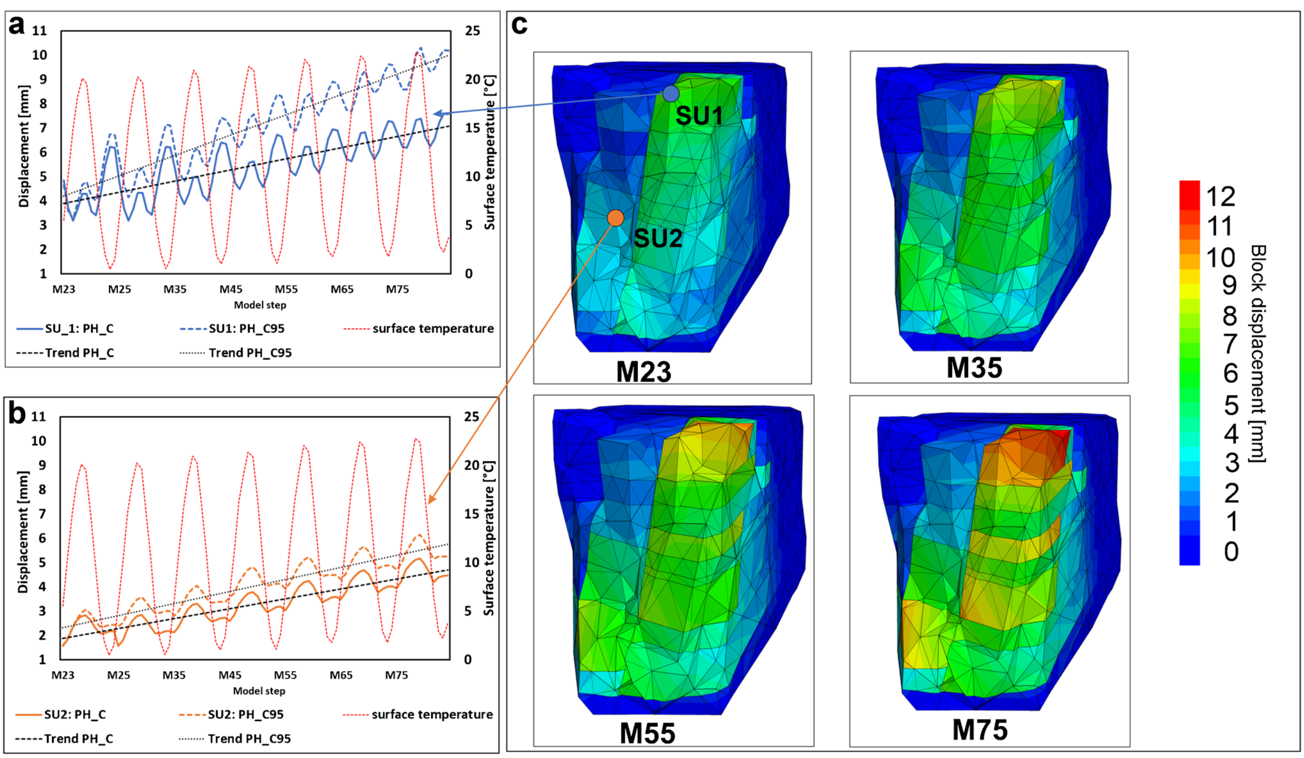

Fig. 6 Monitoring points and model front face displacement. Displacement of history points SU1 (**a**) and SU2 (**b**) in scenarios PH_C and PH_C95. Modelled surface displacement of the front face in scenario PH_C95 (**c**). Results are shown for four time periods: M23 (1995–2025), M35 (2021–2050), M55 (2041–2070), and M75 (2061–2090), from the graphs (**a**, **b**) accelarated ireversable displacement during PH_C95 scenario is observable

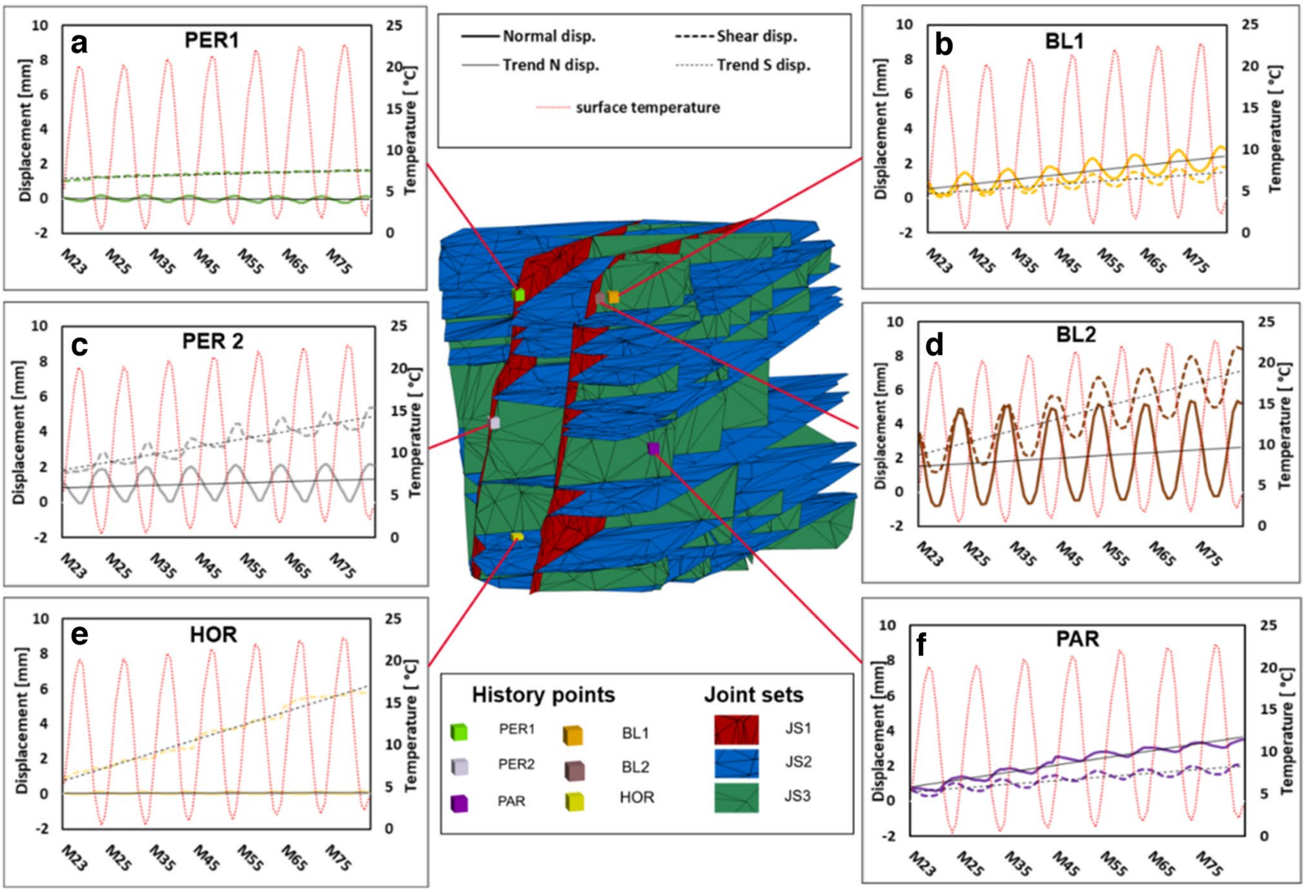

Fig. 7 Temporal evolution of normal and shear displacements at selected history points located within discontinuity sets, based on the results of model PH_C95 (high warming): (**a**) PER1 (JS1, upper slope); (**b**) BL1 (JS3); (**c**) PER2 (JS1, lower slope); (**d**) BL2 (intersection of JS1 and JS3); (**e**) HOR (JS2, sub-horizontal); (**f**) PAR (JS3, parallel to slope face)

and thermally induced volume changes in the near surface. Areas with the highest displacement correspond to regions with persistent and well-developed discontinuities—particularly in the upper left sector of the slope. In contrast, zones where discontinuities are less persistent exhibit significantly lower cumulative displacement.

Similar to the surficial displacement results, the highest overall joint displacements were observed under the PH_C95 scenario. Under PH_NW, joint displacement—particularly joint opening—is more significant during colder periods owing to the thermal contraction of the surrounding rock blocks. This thermal contraction facilitates joint opening in the absence of long-term warming. However, under the PH_C95 scenario, the overall trends in both normal and shear displacements are more pronounced.

Specifically, in terms of normal displacement (Fig. 7), BL2 exhibits a significantly larger annual displacement amplitude than BL1. However, BL1 shows a more pronounced long-term trend, along with an increase in annual amplitude. The average annual amplitude is 1.39 mm for BL1 and 5.53 mm for BL2. The irreversible displacement (Δdisp/1Y) is 0.24 mm for BL1 and 0.10 mm for BL2. Thus, high values of TM-induced normal joint displacement do not necessarily correlate with substantial irreversible joint opening. HOR, located within JS2 in the lower part of the rock slope (Fig. 7e), shows minimal normal displacement amplitude and trend. This limited response is largely due to gravitational confinement from the overlying rock mass. PER1 and PER2 are situated in the upper and lower parts of the slope, respectively, within JS1 and JS3. Here, normal displacement is primarily temperature-driven, with joint opening during colder periods as a result of thermal contraction. For PER1 (Fig. 7a), the average annual amplitude is 0.36 mm, without a discernible long-term trend (Δdisp/1Y = 0.009 mm). Conversely, PER2 (Fig. 7c), located within a joint separating a thin surficial rock block, shows a more significant trend, with an average annual amplitude of 2.02 mm and Δdisp/1Y = 0.05 mm. The location of PER2 within a structurally isolated block subject to both gravitational forces and thermal expansion enhances this behaviour, especially under the PH_C95 scenario. PAR (Fig. 7f), situated within joint set JS3 (oriented parallel to the rock face), shows low annual amplitude (0.27 mm) and an opening trend (Δdisp/1Y = 0.24 mm), suggesting combined effects of gravitational and thermo-mechanical forcing. Under the PH_NW scenario, a reduced degree of joint closure is observed due to the lower thermal expansion of the rock matrix.

The shear displacement patterns of BL1 and BL2 resemble those observed in normal displacement (Fig. 7b,d). Point BL2 shows a higher increment in shear displacement (Δdisp/1Y = 0.65 mm) and an average annual amplitude of 3.56 mm. For BL1, a clear positive trend is also evident, with Δdisp/1Y = 0.16 mm and an annual amplitude of 0.84 mm. At HOR (Fig. 7e), the shear displacement trend is even more pronounced (Δdisp/1Y = 0.73 mm), with an average annual amplitude of 0.5 mm. Both PER1 (Fig. 7a) and PER2 (Fig. 7c) show positive trends in shear displacement. However, PER2 exhibits a higher annual amplitude and displacement trend, reflecting a more dynamic evolution possibly influenced by the detachment of a surficial block. Finally, PAR (Fig. 7f) shows a modest amplitude (0.63 mm) and trend (Δdisp/1Y = 0.2 mm), pointing to a gradual destabilisation of the associated partial block, influenced by both thermal and gravitational forces.

To further assess the displacement trends, the slopes of the linear functions approximating the normal and shear displacement trends were calculated (Table S2). These slope values serve as indicators of irreversible joint displacement. Notably, relatively high slope values were obtained for surficial points SU1 and SU2, as well as for joint points BL1 and PAR, especially under the PH_C95 scenario. Across all monitored points, the slopes of shear displacement trends were generally steeper than those for normal displacement, indicating a shear-dominated deformation mechanism.

An analysis of the mechanical state of joint contacts reveals that already during the mechanical initialisation phase, a considerable number of contact points reached failure under plastic conditions (Fig. 8a), manifesting both in slip and tensile failure modes. Consequently, the modelled blocks are considered fully plastic within joint contacts, though the internal structure of the rock blocks remains entirely elastic. Plastic behaviour is thus limited to the joint interfaces, which are governed by an elasto-plastic model. Slip failures are predominantly concentrated within sub-horizontal joints, while tensile failures tend to localise near the surface in sub-vertical joints. Notably, the number of tensile failures in the lower part of the model increases progressively during the simulation. As the predictive modelling advances through time steps (M23, M55, M75), failures also begin to emerge in the upper part of the model domain (Fig. 8b-d). Comparing the contact state after the mechanical initialisation with that following the thermo-mechanical predictive modelling (Fig. 8c), a contribution of thermal–mechanical forcing to the propagation of plastic failures within the joint network is evident.

Discussion and conclusions

Predictive modelling revealed that future temperature increases can lead to discernible trends in both surface and joint displacements, indicating possible gradual thermo-mechanically driven slope destabilisation, predominantly within the elastic domain. This

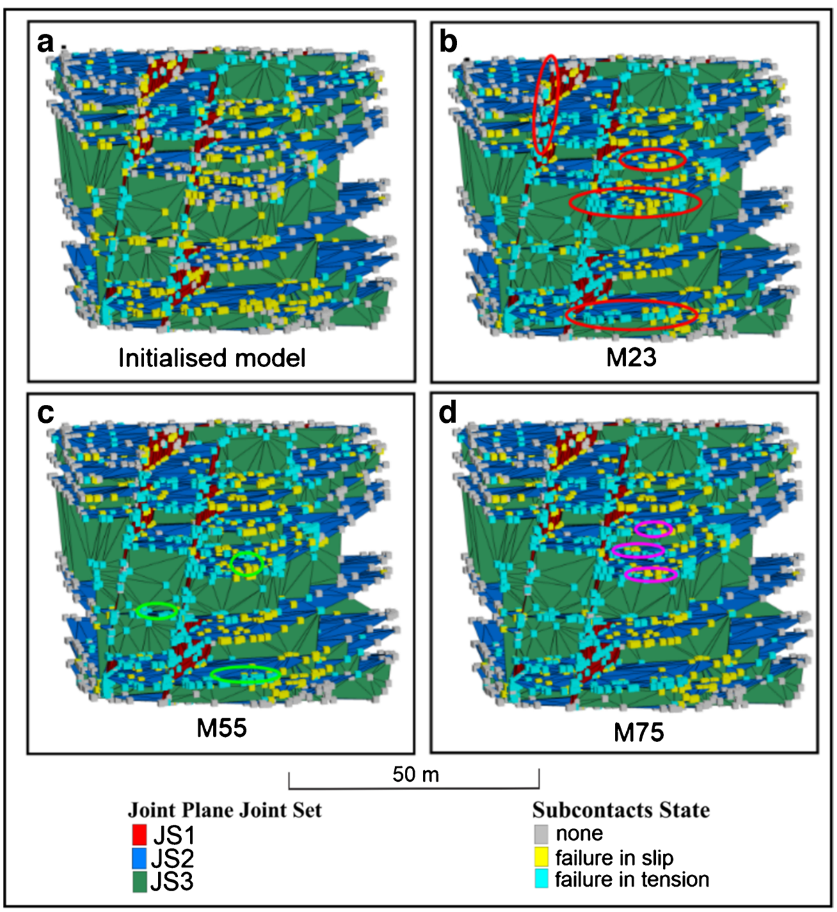

Fig. 8 Evolution of plastic failure within sub-contacts (points along joints separating partial blocks) during the PH_C95 scenario. (**a**) Initial distribution of sub-contacts that failed in plastic deformation after the mechanical initialisation phase. (**b**) Red ovals indicate newly developed plastic failures by model step M23. (**c**) Green ovals highlight additional failures formed between steps M23 and M55. (**d**) Magenta ovals show further propagation of plastic deformation between steps M55 and M75

destabilisation is manifested by observed trends in joint and rock face displacements. The modelled results are consistent with findings from previous studies (Gischig et al. 2011; Marmoni et al. 2020; Morcioni et al. 2022). Laboratory investigations have also examined rock mass behaviour under cyclic thermal loading, revealing trends of rock matrix weakening and influences on discontinuity behaviour (e.g., Kim et al. 2014; Rong et al. 2018). However, direct comparison with the modelling results is limited by differences in spatial and temporal scales. Furthermore, implementing a faster temperature increase scenario resulted in more pronounced displacement trends, highlighting the importance of the climate change rate in accelerating rock slope destabilisation. Nevertheless, the uncertainties and limitations inherent in the modelling approach should be recognised before drawing conclusions.

The model geometry was simplified in terms of surface topography and the configuration of joint sets. A major source of uncertainty lies in the unknown subsurface joint distribution, which cannot be precisely characterised in a model of this scale. Thus, the joint sets in the model should be regarded as conceptual constructs, derived from statistical interpretations of surface mapping and remote sensing data. Consequently, the predictive model should be understood as a simplified, conceptual representation of complex in situ geological conditions.

The calibration of thermal parameters did not account for the influence of three-dimensional heat transfer owing to the limited temporal resolution (one month), which prevented the capture of diurnal and seasonal variations in solar radiation. Thus, some discrepancies emerged between measured and modelled subsurface temperatures. Overestimation of λ led to steeper heating curves, while increased C_P values resulted in less dampening of the temperature amplitude across all depths. The choice of thermal expansion coefficient (α) influenced the modelled joint normal displacement. Variations in Young's modulus (E) significantly impacted the amplitude of joint displacement. In contrast, Poisson's ratio (ν) had a limited influence. Adjustments in joint stiffness influenced both the amplitude and temporal pattern of joint displacements, highlighting the necessity of accurately characterising this parameter to simulate realistic displacement dynamics under thermo-mechanical loading. Regarding the mechanical calibration, it is important to note that it was conducted using data from a single crackmeter. However, since the crackmeter was installed perpendicular to the crack, a direct comparison with the modelled displacement was possible. No significant trend was observed in the measurements over six years, indicating that primarily the thermal expansion or dilatation of the block had been recorded. To enhance the model calibration, it would be beneficial to install multiple crackmeters or strain gauges to measure the thermal expansion of the rock surface.

Uncertainties in the thermal component of the model may arise from simplifications related to the representation of the rock matrix during temperature probe data modelling. Inhomogeneities within the rock matrix, which can significantly affect heat transfer, were not considered. Furthermore, seasonal variations in water content within the rock mass can substantially influence thermal conductivity in the surficial zone; however, due to the lack of data, this effect was neglected. Notably, the limited temporal resolution also affected the model's ability to account for short-term forcing (e.g., heatwaves or wildfires) that may influence the behaviour of the surficial layer, particularly in rapid destabilisation or triggering events (Collins and Stock 2016). Addressing diurnal cycles would require a distinct modelling approach with higher temporal granularity. This remains an important direction for future investigation.

A further limitation comes from the modelling approach, where the 70-year evolution of the rock slope was represented by seven generalised annual thermal cycles. The choice was driven by the limited temporal resolution of future climate datasets and the high computational demands. However, this may have led to an underestimation of the total magnitude of thermally induced displacement.

The reliability of predictive modelling also depends on the accuracy of climate model outputs. While climate models generally perform well over large spatial domains, their downscaling to specific regions or individual slopes introduces uncertainties (Serifi et al. 2021) that propagate into the model outcomes. Consequently, the results should be primarily interpreted in terms of overall trends in slope evolution rather than relying on absolute displacement values.

Despite the inherent uncertainties and limitations of the modelling approach, several insights can be gained, namely that: (i) calibration and reliability of thermo-mechanical models can be enhanced by integrating diverse monitoring data; (ii) considering the three-dimensional geometry of the rock slope is essential during thermal calibration, as it controls heat transfer within the rock matrix; (iii) annual temperature cycles produce measurable joint displacements, primarily driven by thermo-mechanical expansion and dilation of partial rock slope blocks; (iv) climate change can induce irreversible joint displacements through increasing temperatures, accelerating mechanical degradation. Overall, it can be concluded that enhanced temperature cycles can be a preparatory factor in the destabilisation of rock slopes, potentially contributing to the timing and occurrence of rockfalls.

Acknowledgements

The authors wish to thank Charles University and the Czech Academy of Sciences for their financial support. We would also like to thank the reviewer for their comments and notes, which led to improvements in this paper.

Funding

This research was performed in the framework of the long-term conceptual development research organisation RVO: 67985891. This research was supported by the Johannes Amos Comenius Programme (P JAC), project No. CZ.02.01.01/00/22_008/0004605, Natural and anthropogenic georisks, and the Czech Science Foundation project n. 25-17664S.

Data Availability

All relevant data are available in the article, the supplementary information file, and from referenced literature. ITASCA 3DEC 9.0 (www.itascasoftware.com) and COMSOL Multiphysics 5.4 software (www.comsol.com) were used under licenses purchased by the University of Milan within the PhD programme of Andrea Morcioni. CloudCompare is a free open-source software with a GNU General

Public License (https://www.cloudcompare.org/). DSE – Discontinuity Set Extractor is a free MATLAB programme available from the University of Alicante (https://personal.ua.es/en/ariquelme/dse-discontinuity-set-extractor.html).

Declarations

Conflict of interest The authors declare no competing interests.

References

Allen S, Huggel C (2013) Extremely warm temperatures as a potential cause of recent high mountain rockfall. Glob Planet Change 107:59–69
ASTM (2002) D3148 Standard Test Method for elastic moduli of intact rock core specimens in uniaxial compression. https://store.astm.org/d3148-02.html. Accessed 20 Mar 2025
Balkan E, Erkan K, Şalk M (2017) Thermal conductivity of major rock types in western and central Anatolia regions, Turkey. J Geophys Eng 14:909–919
Barton N (1976) The shear strength of rock and rock joints. International Journal of Rock Mechanics and Mining Sciences & Geomechanics Abstracts 13:255–279
Blahůt, J., Racek, O. (2023) Modern methods of rock mass characterisation and rockfall monitoring: a review. In: Thambidurai, P., Singh, T.N. (eds) Landslides: detection, prediction and monitoring. Springer, Cham. https://doi.org/10.1007/978-3-031-23859-8_1
Blikra LH, Christiansen HH (2014) A field-based model of permafrost-controlled rockslide deformation in northern Norway. Geomorphology 208:34–49
Bolla A, Paronuzzi P (2020) Numerical investigation of the pre-collapse behavior and internal damage of an unstable rock slope. Rock Mech Rock Eng 53:2279–2300
Brideau M-A, Pedrazzini A, Stead D et al (2011) Three-dimensional slope stability analysis of South Peak, Crowsnest Pass, Alberta, Canada. Landslides 8:139–158
Čech S (2011) Palaeogeography and stratigraphy of the Bohemian Cretaceous Basin (Czech Republic) – an overview. Geologické výzkumy (na Moravě a ve Slezsku), 18(1).
Cílek V (2009) Saxon-Bohemian Switzerland: sandstone rock cities and fascination in a romantic landscape. Geomorphological Landscapes of the World 201–209. https://doi.org/10.1007/978-90-481-3055-9_21
Collins BD, Stock GM (2016) Rockfall triggering by cyclic thermal stressing of exfoliation fractures. Nat Geosci 9:395–400
Collins BD, Stock GM, Eppes M-C et al (2018) Thermal influences on spontaneous rock dome exfoliation. Nat Commun 9:762
D'Amato J, Hantz D, Guerin A et al (2016) Influence of meteorological factors on rockfall occurrence in a middle mountain limestone cliff. Nat Hazards Earth Syst Sci 16:719–735
Deng Y, Fan X, Scaringi G et al (2023) Effect of particle crushing– and thermally induced pressurization on rockslide mobility. Landslides 20:1535–1546
Desai PD, Navarro RA, Hasan SE, et al (1974) Thermophysical properties of selected rocks. CINDAS Report 23:
Do Amaral Vargas E, Velloso RQ, Chávez LE et al (2013) On the effect of thermally induced stresses in failures of some rock slopes in Rio de Janeiro, Brazil. Rock Mech Rock Eng 46:123–134
Donati D, Stead D, Stewart TW, Marsh J (2020) Numerical modelling of slope damage in large, slowly moving rockslides: insights from the Downie Slide, British Columbia, Canada. Eng Geol 273:105693
Emirov SN, Aliverdiev AA, Zarichnyak YP, Emirov RM (2021) Studies of the effective thermal conductivity of sandstone under high pressure and temperature. Rock Mech Rock Eng 54:3165–3174
Eppes MC, Magi B, Hallet B et al (2016) Deciphering the role of solar-induced thermal stresses in rock weathering. Geol Soc Am Bull 128:1315–1338. https://doi.org/10.1130/B31422.1
Fan X, Xu Q, Scaringi G et al (2017) Failure mechanism and kinematics of the deadly June 24th 2017 Xinmo landslide, Maoxian, Sichuan, China. Landslides 14:2129–2146
Fan X, Xu Q, Scaringi G et al (2019) The "long" runout rock avalanche in Pusa, China, on August 28, 2017: a preliminary report. Landslides 16:139–154
Fiorucci M, Marmoni GM, Martino S, Mazzanti P (2018) Thermal response of jointed rock masses inferred from infrared thermographic surveying (Acuto test-site, Italy). Sensors 18:2221
Gischig VS, Moore JR, Evans KF et al (2011) Thermomechanical forcing of deep rock slope deformation: 1. Conceptual study of a simplified slope. J Geophys Res 116(F4):4010
Gischig V, Preisig G, Eberhardt E (2016) Numerical investigation of seismically induced rock mass fatigue as a mechanism contributing to the progressive failure of deep-seated landslides. Rock Mech Rock Eng 49:2457–2478
Grämiger LM, Moore JR, Gischig VS, Loew S (2018) Thermomechanical stresses drive damage of Alpine valley rock walls during repeat glacial cycles. J Geophys Res Earth Surf 123:2620–2646
Guillemot A, Baillet L, Larose E, Bottelin P (2022) Changes in resonance frequency of rock columns due to thermoelastic effects on a daily scale: observations, modelling and insights to improve monitoring systems. Geophys J Int 231:894–906
Hall K (1999) The role of thermal stress fatigue in the breakdown of rock in cold regions. Geomorphology 31:47–63
Harris C, Arenson LU, Christiansen HH et al (2009) Permafrost and climate in Europe: monitoring and modelling thermal, geomorphological and geotechnical responses. Earth-Sci Rev 92:117–171
Hoek E, Brown ET (1997) Practical estimates of rock mass strength. Int J Rock Mech Min Sci 34:1165–1186
Hormes A, Adams M, Amabile AS et al (2020) Innovative methods to monitor rock and mountain slope deformation. Geomech Tunnell 13:88–102
ISRM, (1978) Suggested methods for the quantitative description of discontinuities in rock masses. (Coordinator, Barton, N.) International Journal of Rock Mechanics and Mining Science and Geomechanics Abstracts, Vol. 15, pp. 319–368.
Kim K, Kemeny J, Nickerson M (2014) Effect of rapid thermal cooling on mechanical rock properties. Rock Mech Rock Eng 47:2005–2019
Lan H, Martin CD, Andersson JC (2013) Evolution of in situ rock mass damage induced by mechanical–thermal loading. Rock Mech Rock Eng 46:153–168
Magnin F, Deline P, Ravanel L et al (2015) Thermal characteristics of permafrost in the steep alpine rock walls of the Aiguille du Midi (Mont Blanc Massif, 3842 m a.s.l). Cryosphere 9:109–121
Mamot P, Weber S, Eppinger S, Krautblatter M (2021) A temperature-dependent mechanical model to assess the stability of degrading permafrost rock slopes. Earth Surf Dyn 9:1125–1151
Marmoni GM, Fiorucci M, Grechi G, Martino S (2020) Modelling of thermo-mechanical effects in a rock quarry wall induced by near-surface temperature fluctuations. Int J Rock Mech Min Sci 134:104440

Meitner J, Štěpánek P, Skalák P et al (2023) Validation and selection of a representative subset from the ensemble of EURO-CORDEX EUR11 regional climate model outputs for the Czech Republic. Atmosphere 14:1442

Mirhadi N, Macciotta R (2023) Quantitative correlation between rock fall and weather seasonality to predict changes in rock fall hazard with climate change. Landslides 20:2227–2241

Morcioni A, Apuani T, Cecinato F (2022) The role of temperature in the stress–strain evolution of Alpine rock-slopes: thermo-mechanical modelling of the Cimaganda rockslide. Rock Mech Rock Eng 55:2149–2172

Ozudogru TY, Olgun CG, Senol A (2014) 3D numerical modeling of vertical geothermal heat exchangers. Geothermics 51:312–324

Pasten C, García M, Cortes DD (2015) Physical and numerical modelling of the thermally induced wedging mechanism. Geotech Lett 5:186–190

Racek O, Blahut J, Hartvich F (2021) Observation of the rock slope thermal regime, coupled with crackmeter stability monitoring: initial results from three different sites in Czechia (central Europe). Geosci Instrum Method Data Syst 10:203–218

Racek, O., Blahůt, J. (2023) Rock mass characterization and rockfall monitoring: traditional approaches. In: Thambidurai, P., Singh, T.N. (eds) Landslides: Detection, Prediction and Monitoring. Springer, Cham. https://doi.org/10.1007/978-3-031-23859-8_2

Rafiee R, Ataei M, KhalooKakaie R et al (2018) Numerical modeling of influence parameters in cavabililty of rock mass in block caving mines. Int J Rock Mech Min Sci 105:22–27

Ravandi EG, Rahmannejad R, Monfared AEF, Ravandi EG (2013) Application of numerical modeling and genetic programming to estimate rock mass modulus of deformation. Int J Min Sci Technol 23:733–737

Riquelme AJ, Tomás R, Abellán A (2016) Characterization of rock slopes through slope mass rating using 3D point clouds. Int J Rock Mech Min Sci 84:165–176

Rong G, Peng J, Cai M et al (2018) Experimental investigation of thermal cycling effect on physical and mechanical properties of bedrocks in geothermal fields. Appl Therm Eng 141:174–185

Salmon F, Lacanette D, Lharti H, Sirieix C (2023) Heat transfer in rock masses: application to the Lascaux Cave (France). Int J Heat Mass Transf 207:124029

Scaringi G, Loche M (2022) A thermo-hydro-mechanical approach to soil slope stability under climate change. Geomorphology 401:108108

Serifi A, Günther T, Ban N (2021) Spatio-temporal downscaling of climate data using convolutional and error-predicting neural networks. Front Clim 3:656479

Stoffel M, Huggel C (2012) Effects of climate change on mass movements in mountain environments. Prog Phys Geogr 36:421–439

Sundberg J (1988) Thermal properties of soils and rocks. Dissertation, Chalmers University of Technology and University of Göteborg

Tourchi S, Manica MA, Gens A et al (2025) A thermomechanical model for argillaceous hard soils-weak rocks: application to THM simulation of deep excavations in claystone. Geotech 75(2):139–152

Vařilová Z, Podroužek K, Belisová N, Horák J (2022) Stability deterioration of cliff faces due to historical mining in the Elbe sandstones protected area. Stavební Obzor-Civ Eng J 31:516–532

Wang F, Konietzky H, Frühwirt T, Dai Y (2020) Laboratory testing and numerical simulation of properties and thermal-induced cracking of Eibenstock granite at elevated temperatures. Acta Geotech 15:2259–2275

Wu Z, Zhou Y, Weng L et al (2020) Investigation of thermal-induced damage in fractured rock mass by coupled FEM-DEM method. Comput Geosci 24:1833–1843

Wyllie DC, Mah CW (2017) Rock slope engineering: Civil and mining, 4th edition. Rock Slope Engineering: Fourth Edition 1–432.

Yu H, Chen W, Ma Y, Gong Z, Lu H (2023) Thermo-mechanical effect on the drained creep behavior of a clay rock. Eng. Geol. 327:107327

Zajíc J (1977) Stabilization of the rock wall'Pastýřská stěna'by anchoring. Bull. Eng. Geol. Environ. 16:180–183

Zhao S, He S, Li X et al (2024) Investigating the dynamic process of a rock avalanche through an MLS-MPM simulation incorporated with a nonlocal μ(I) rheology model. Landslides 21:1483–1499

Zhou X, Xu Y (2021) A new thermal analysis model with three heat conduction layers in the nuclear waste repository. Nucl. Eng. Des. 371:110929

Supplementary Information The online version contains supplementary material available at https://doi.org/10.1007/s10346-025-02659-9.

Ondřej Racek (✉) · Jan Blahůt
Department of Applied Rock Mechanics, Institute of Rock Structure and Mechanics, Czech Academy of Sciences, V Holešovickách 94/41, 182 09 Prague, Czechia
Email: racek@irsm.cas.cz

Ondřej Racek
Department of Physical Geography and Geoecology, Charles University, 128 00 Prague, Czechia

Andrea Morcioni · Tiziana Apuani
Dipartimento di Scienze Della Terra 'A. Desio', Università degli Studi di Milano, Via Mangiagalli, 34, 20133 Milan, Italy

Petr Štěpánek
Global Change Research Institute (Czech Globe), Czech Academy of Sciences, 603 00 Brno, Czechia

Gianvito Scaringi
Institute of Hydrogeology, Engineering Geology and Applied Geophysics, Faculty of Science, Charles University, 128 00 Prague, Czechia